ULTRA-FAINT ULTRAVIOLET GALAXIES AT $Z \sim 2$ BEHIND THE LENSING CLUSTER ABELL 1689: THE LUMINOSITY FUNCTION, DUST EXTINCTION AND STAR FORMATION RATE DENSITY[1]

Anahita Alavi, Brian Siana[2], Johan Richard[3], Daniel P. Stark[4], Claudia Scarlata[5], Harry I. Teplitz[6], William R. Freeman[2], Alberto Dominguez[2], Marc Rafelski [6], Brant Robertson[4], Lisa Kewley[7]
Draft Version, April, 2013

ABSTRACT

We have obtained deep ultraviolet imaging of the lensing cluster Abell 1689 with the WFC3/UVIS camera onboard the *Hubble Space Telescope* in the F275W (30 orbits) and F336W (4 orbits) filters. These images are used to identify $z \sim 2$ star-forming galaxies via their Lyman break, in the same manner that galaxies are typically selected at $z \geq 3$. Because of the unprecedented depth of the images and the large magnification provided by the lensing cluster, we detect galaxies 100× fainter than previous surveys at this redshift. After removing all multiple images, we have 58 galaxies in our sample between $-19.5 < M_{UV} < -13$. Because the mass distribution of Abell 1689 is well constrained, we are able to calculate the intrinsic sensitivity of the observations as a function of source plane position, allowing for accurate determinations of effective volume as a function of luminosity. We fit the faint-end slope of the luminosity function with our data alone to be $\alpha = -1.56 \pm 0.13$, somewhat shallower than the values obtained at $z > 3$. Notably, there is no turnover in the luminosity function down to $M_{UV} = -13$. We fit the UV spectral slopes with photometry from existing *Hubble* optical imaging. The observed trend of increasingly redder slopes with luminosity at higher redshifts is observed in our sample, but with redder slopes at all luminosities and average reddening of $< E(B-V) >= 0.15$. We assume the stars in these galaxies are metal poor ($0.2Z_\odot$) compared to their brighter counterparts ($Z_\odot$), resulting in bluer assumed intrinsic UV slopes and larger derived values for dust extinction. The total UV luminosity density at $z \sim 2$ is 4.3×10^{26} erg s^{-1} Hz^{-1} Mpc^{-3}, 80% of which is emitted by galaxies in the luminosity range of our sample. Finally, we determine the global star formation rate density from UV-selected galaxies at $z \sim 2$ (assuming a constant dust extinction correction of 4.2 over all luminosities and a Kroupa IMF) of 0.147 M$_\odot$ yr^{-1} Mpc^{-3}, significantly higher than previous determinations because of the additional population of fainter galaxies and the larger dust correction factors.

Subject headings: galaxies: evolution – galaxies: high-redshift – galaxies: luminosity function, mass function

1. INTRODUCTION

A primary goal of observational cosmology has been to obtain a complete census of star formation at all epochs (e.g, Madau et al. 1996; Lilly et al. 1996). One effective method of selecting star-forming galaxies is to identify a "Lyman break" in the ultraviolet (UV) continuum caused by Lyman line and continuum absorption from hydrogen in the stellar atmospheres, interstel-

lar medium, and the intergalactic medium (Steidel et al. 1999). This technique was first used to select the star-forming galaxies as U-band "dropouts" at z~3 (Steidel et al. 1999), and has since been widely adopted to select Lyman break galaxies (LBGs) at higher redshifts (e.g., Bunker et al. 2004; Sawicki & Thompson 2006; Yan et al. 2006; Bouwens et al. 2007, 2009; Reddy & Steidel 2009; Oesch et al. 2010b; Bunker et al. 2010; Yan et al. 2010; Hathi et al. 2012).

Although the peak epoch of star formation is likely at lower redshifts ($1.5 < z < 3$, Reddy & Steidel 2009), it has been impossible to select galaxies via their Lyman break without imaging at wavelengths below the atmospheric limit, $\lambda < 3100$ Å. Other selection methods like the BM/BX (Adelberger et al. 2004) and BzK (Daddi et al. 2004) criteria have been used, but unambiguous comparison with Lyman break selected galaxies at $z \geq 3$ is difficult due to selection effects.

The new Wide–Field Camera 3 (WFC3) on the *Hubble Space Telescope* has an ultraviolet/optical channel (UVIS) that increases survey efficiency (area × throughput) by more than an order of magnitude. With the first ultraviolet images in the Early Release Survey (ERS) (Windhorst et al. 2011), star-forming galaxies were selected via the Lyman break technique at $1 < z < 3$ (Oesch et al. 2010a; Hathi et al. 2010). These studies

were limited by the depth of the shallow ultraviolet imaging and could only detect galaxies with $M_{UV} > -19$, making it impossible to accurately constrain the faint-end slope of the UV luminosity function (LF).

The rest-frame ultraviolet light is a strong tracer of star formation, so the UV luminosity function can be used to determine the relative contribution of faint and bright galaxies to the total star formation rate density (SFRD). The UV LF has been studied widely at this active star forming era (Arnouts et al. 2005; Reddy & Steidel 2009; Hathi et al. 2010; Oesch et al. 2010a).

There are two difficulties in determining a complete census of star formation. First, the ultraviolet light in bolometrically luminous galaxies is significantly attenuated by dust, which causes UV-selected samples to be incomplete at the bright end. However, these galaxies can be identified by their far-infrared emission (Reddy et al. 2006; Magnelli et al. 2011). Second, there may be a large population of faint star-forming galaxies beyond the detection limit of our deepest surveys (typically $M_{UV} < -18$).

This population of faint ultraviolet galaxies may contribute significantly to the global star formation density and the ionizing background (Nestor et al. 2012) at $z > 2$. Recent searches at z=3 (Nestor et al. 2011) have revealed that the faint star-forming galaxies on average have larger Lyman continuum escape fraction relative to the brighter galaxies. This result proves the importance of these feeble objects in maintaining the ionizing emissivity especially at the peak of star formation activity. They may also be the currently undetected hosts of many gamma-ray bursts (GRBs) (Robertson & Ellis 2012; Tanvir & Levan 2012; Trenti et al. 2012). In addition to the crucial role of the faint galaxies at lower redshifts, it is believed that low luminosity galaxies at $z > 7$ are likely the primary sources of ionizing photons that caused the reionization of the intergalactic medium (Kuhlen & Faucher-Giguère 2012; Robertson et al. 2013). Studying an analogous population at lower redshifts ($z \sim 2$) provides us a more clear picture of ultra-faint populations at high redshifts.

One way to efficiently detect and study these faint galaxies is to use foreground massive systems as lenses to magnify background galaxies. This strong gravitational lensing conserves surface brightness while spreading out a galaxies' light over a larger area, effectively magnifying it. Over the last decade, this has been used to study individual lensed galaxies in great detail (e.g., Pettini et al. 2002; Siana et al. 2008a, 2009; Stark et al. 2008; Jones et al. 2010; Yuan et al. 2013).

When using strong lensing to identify large numbers of faint galaxies, galaxy clusters are particularly useful as they highly magnify background galaxies over a large area (Narayan et al. 1984). The regions amplified by a higher factor have smaller source-plane area, so the benefit of magnification is offset by reduced sample volume. Therefore the total number of candidate galaxies behind a cluster would be either smaller or larger than a field survey due to the competition between the area and the depth. Determining the overall advantage of using cluster lensing relative to the field studies depends on the effective slope of the luminosity function (Broadhurst et al. 1995; Bouwens et al. 2009). If the effective slope of the luminosity func-

tion ($-d(\log d\phi)/d\log L$) is greater than unity then a survey behind a lensing cluster will find more objects than the same survey in the field. Lensing clusters have been used to identify very high redshift objects (Kneib et al. 2004; Egami et al. 2005; Stark et al. 2007; Bradley et al. 2008; Richard et al. 2008; Bouwens et al. 2009; Richard et al. 2011; Bouwens et al. 2012a; Zheng et al. 2012; Zitrin et al. 2012; Coe et al. 2013) because the luminosities probed are on the steep, bright end of the luminosity function, resulting in larger samples than field surveys. Historically, surveys have not used lensing clusters to identify galaxies significantly fainter than L^* because it finds fewer galaxies. However, our primary concern is not the *number* of galaxies found, but the intrinsic *luminosity* of the galaxies. The average luminosity of galaxies found behind a lensing cluster will be significantly lower than surveys in the field. Because we are interested in finding galaxies that are undetected in our deepest field surveys, we chose to survey faint star-forming galaxies behind massive clusters. Once these ultra-faint galaxies are identified, the lensing will allow detailed study as they are highly magnified and the light is spread over many more resolution elements. This strategy of surveying large numbers of background galaxies with deep observations of lensing clusters will soon be adopted with deep *Hubble* imaging of the Frontier Fields beginning in Cycle 21.

In this paper we use the WFC3/UVIS channel to look for faint galaxies located behind the massive cluster Abell 1689. This cluster has the most constrained cluster mass model due to the large number of confirmed multiply imaged systems (43), of which 24 have spectroscopic redshifts (Limousin et al. 2007; Coe et al. 2010). This mass model gives us a precise estimation of magnification factor over the total area. The high magnification area for this cluster is well-matched with the WFC3/UVIS field of view. Abell 1689 has been observed extensively with HST in the optical with ACS/WFC (F475W, F625W, F775W, F850LP, F814W) and the near-IR with WFC3/IR (F105W, F125W, F140W, F160W) as well as Spitzer IRAC/MIPS and Herschel PACS/SPIRE.

The outline of this paper is as follows. In Section 2, we describe the observations and data reduction. The selection technique is given in Section 3. Then in Section 4 we talk about the details of the completeness simulation as well as the Monte Carlo simulation used for IGM opacity. We explain the two methods used for estimating the rest-frame UV luminosity function parameters in Section 5. In Section 6 we determine the dust content of the selected Lyman break galaxies. In Section 7, we compare our final results for the UV luminosity density and evolution of the faint-end slope and dust extinction with other results in the literature. We also briefly discuss about the effect of the intracluster dust. Finally, we present a short summary in Section 8.

All magnitudes are in AB units (Oke & Gunn 1983). We assume $\Omega_M = 0.3$, $\Omega_\Lambda = 0.7$ and $H_\circ = 70$ km s^{-1} Mpc^{-1}.

2. OBSERVATIONS

We targeted the massive, rich cluster Abell 1689, behind which we are looking for the faint star-forming galaxies (HST Program ID 12201, PI: B. Siana). We used the WFC3 UVIS channel to obtain images in F275W (30

orbits) and F336W (4 orbits). The data were obtained between December, 2010 and March, 2011. We used long exposure times, half an orbit in length (1310s each) in order to minimize the total read noise, as this is the dominant source of noise in near-UV imaging with *Hubble.* The data were obtained in two orbit visits during which we performed the standard UVIS dither pattern, WFC3-UVIS-DITHER-BOX. Each dither pattern was offset up to ± 3" from the central pointing to place different pixels on the same objects and to fully cover the UVIS chip gap. The 5σ depths measured in a $0.2''$ radius aperture are given in Table 1.

In order to identify the LBGs at $z \sim 2$, we also used the existing HST/ACS images in optical bands (F475W, F625W, F775W, F850LP; PID 9289, PI: H. Ford). Table 1 shows the limiting magnitudes of these observations. The overlapping area between the ACS and WFC3/UVIS fields of view, after subtracting the areas contaminated by the bright cluster galaxies, covers 6.56 arcmin^2 in the image plane.

2.1. *Data Reduction*

The calibrated, flat fielded WFC3/UVIS and ACS images were processed with *MultiDrizzle* (Koekemoer et al. 2003), part of the STSDAS/DITHER iraf package. The initial drizzled images were registered to SDSS images in order to compute the shift file required for astrometric correction. The ACS and UVIS images in different bands are taken in sub-pixel dithered visits, so we made a shift file for each visit to project all the images to the same astrometric reference grid.

The F336W image was aligned with the SDSS g'-band image with an accuracy of $0.1''$, using unsaturated stars and compact objects. We chose to use the UVIS F336W image to align with SDSS because many of the stars were not saturated at these wavelengths and the galaxies were generally more compact, resulting in better alignment precision.

The other HST images were matched to F336W to achieve astrometric registration with the SDSS reference frame. The relative alignment of images was done with an accuracy of better than 0.1 pixels ($0.004''$) because of its importance in doing matched-aperture photometry in all filters. The shift files were created by running the *geomap* task in IRAF. These shift files were then used as input to re-run *MultiDrizzle.*

The input images to the *MultiDrizzle* software were drizzled onto separate undistorted output frames which were combined later into a median image. The median image was transformed back (blotted) to the original distorted images in order to make the cosmic ray masks. The final output is a registered, undistorted and cosmic ray-rejected image. We also set *MultiDrizzle* to produce an inverse variance weight image (IVM) to be used for computing errors in the photometry. In order to do matched-aperture photometry for all wavelengths, we set the same output pixel sizes for UVIS and ACS images to $0.04''$. We set the pixfrac to 0.8 for ACS and 1 for UVIS images since these pixfrac values were well matched to our output pixel scale.

The sources were detected in the ACS B band image (F475W) using *SExtractor* (Bertin & Arnouts 1996). The photometry was done by running *SExtractor* in dual image mode using the weight map RMS-MAP gener-

ated by *MultiDrizzle.* We used isophotal apertures with detection threshold 1.27σ and minimum area 16 pixels. We ran *SExtractor* with high and low values for the deblending minimum contrast parameter without changing other parameters in the *SExtractor* configuration file. We were able to detect very faint galaxies as separate objects in the catalog with very low DEBLEND-MINCONT and then add them to the other catalog produced with the larger DEBLEND-MINCONT parameter. This method is similar to hot and cold detections used in Rix et al. (2004). All of the isophotal magnitudes are given in AB magnitudes by using the WFC3 and ACS photometric zero points provided by STScI.

The output errors from *SExtractor* are corrected for the correlated noise (Casertano et al. 2000) because the output pixels in drizzled images are not independent of each other. The correction factor, which is approximately the ratio between uncorrelated noise and correlated errors from *SExtractor*, can be estimated as below:

$$\sqrt{F_A} = \begin{cases} \frac{s}{p}(1 - \frac{1}{3}\frac{s}{p}) & s < p \\ 1 - \frac{1}{3}\frac{p}{s} & s > p \end{cases} \quad (1)$$

where p is the pixfrac and s is the ratio of output pixel size to original pixel size.

3. COLOR SELECTION AND SAMPLE

Neutral hydrogen in galaxies and in the IGM generates a "Lyman break" in the rest-frame UV spectral energy distribution (SED). The Lyman break has long been identified in optical filters to find $z > 3$ galaxies (Steidel et al. 1995). These same optical filters have also been used to find star-forming galaxies in the redshift range $1 < z < 3$ through the absence of a strong break in the blue UV continuum(Adelberger et al. 2004), but that selection is not analogous to the pure Lyman break selection for $z > 3$. Thus, there could be different biases and incompleteness in two samples.

With our near-UV images we can apply the same Lyman break selection to $z \sim 2$ galaxies, allowing for direct comparison with $z \geq 3$ studies. The selection region is defined by the location of star-forming SEDs in color-color space. Our selection criteria, which are shown in Figure 1, were found by running Bruzual & Charlot (2003) (hearafter BC03) models with constant star formation for 100 Myr, reddened by applying Calzetti attenuation curve (Calzetti et al. 2000) with $E(B - V) = \{0, 0.1, 0.2, 0.3\}$ and IGM obscuration from Madau (1995). The green dashed line is the track of lower redshift elliptical galaxies which is extended to $z = 0.2$, as Abell 1689 is at $z = 0.18$.

The color selection criteria for finding the F275W dropouts are:

$$F275W - F336W > 1$$

$$F336W - F625W < 1.3$$

$$F275W - F336W > 2.67(F336W - F625W) - 1.67$$

$$S/N(F336W) > 5 \quad , \quad S/N(F625W) > 5$$

$$(2)$$

We found 84 UV-dropouts using these criteria. Four candidates were dismissed as they were fainter than

Table 1
WFC3/UVIS and ACS Magnitude Limits

Filter	F275W	F336W	F475W	F625W	F775W	F850LP
Magnitude Limit[a]	28.7	27.90	28.55	28.29	28.17	27.80

[a] 5σ limit in a $0.2''$ radius aperture
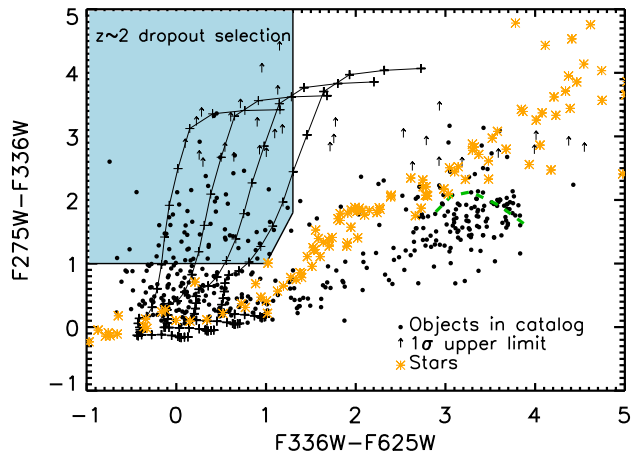
Figure 1. Color selection of $z \sim 2$ Lyman-break galaxies (F275W-dropouts). Black dots are all objects detected at greater than 5σ significance in F336W and F625W filters. Black arrows represent the 1σ upper limit. Black lines are the tracks of star-forming galaxies that are dust obscured with E(B-V)={0, 0.1, 0.2, 0.3}. Orange asterisks are stars from Pickles (1998). The blue shaded region is the region selected by the criteria given in Equation 2. The green dashed line is the expected color track for lower redshift $(0.0 < z < 0.2)$ elliptical galaxies.(Coleman et al. 1980). Abell 1689 is at $z = 0.18$. The large number of red galaxies (in both colors) is primarily due to Abell 1689 cluster galaxies.
(A color version of this figure is available in the online journal)

the limiting magnitude in Table 1 ($U_{336} = 27.9$ and $B_{475} = 28.55$). Because of the strong lensing phenomena, many systems will be multiply imaged and all but one of the images need to be removed from the sample. We removed all of the previously known multiple images (12) except the brightest image in each system. In addition to these confirmed multiple images, the Abell 1689 mass model predicts all of the possible counterimages for each object as a function of redshift. Using these predictions, we found eight new multiple images by performing a visual inspection considering the photometric redshift of each object (A. Dominguez et al., in preparation). We removed two objects with photometric redshifts less than 1.3. Our final sample consists of 58 $z \sim 2$ LBG candidates (see Section 4).

The selected Lyman break galaxies have observed B-band magnitude down to $B < 27.5$, but are intrinsically fainter as they are all highly magnified. The lensing cluster mass model estimates the magnification value at each point of the image as a function of redshift. The magnification of each LBG was measured by assuming an average $z = 2$ (Section 4) for the sample. Figure 2 shows the distribution of magnification in flux units for all the UV-dropout galaxies. The fluxes are on average magnified by a factor of 10 and at some points the magnification becomes incredibly large (up to 100). The distribution of magnification over the whole area of the source plane at $z = 2$ is given in Figure 2 (inset) that shows all the
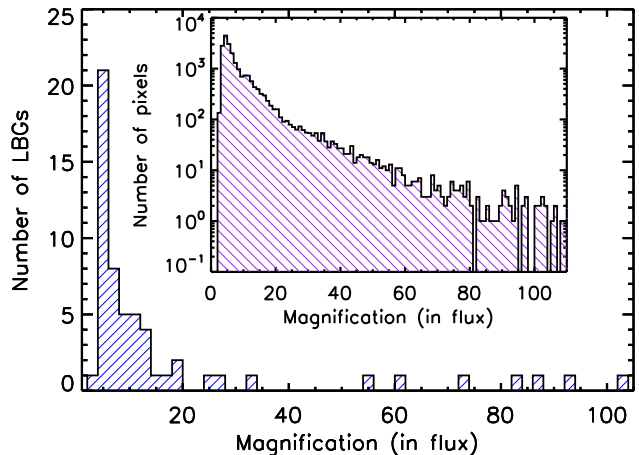
Figure 2. The magnification distribution function of detected $z \sim 2$ Lyman-break galaxies. The magnification values are from the cluster lens model assuming an average redshift $z = 2$ for all the LBGs. The inset shows the distribution function of magnification values over all pixels in the source plane at $z = 2$.
(A color version of this figure is available in the online journal)

pixels in the area are magnified by at least a factor of 2.5 (one magnitude).

Due to the large magnifications, the intrinsic absolute magnitudes probed in this study go down to very faint magnitudes ($M_{1500} < -13$), about 100 times fainter than previous studies ($M_{1500} < -18$) at the same redshift (Reddy & Steidel 2009; Hathi et al. 2010; Oesch et al. 2010a). The intrinsic absolute magnitudes corrected for magnification (M_{1500}) versus observed B-band magnitudes (F475W) are plotted in Figure 3. There are 40 galaxies within the blue box which are both intrinsically very faint (MUV > -18) and bright enough ($B < 26.5$) due to magnification to get ground-based spectroscopy in the rest-frame UV and optical bands.

4. COMPLETENESS

The completeness correction factor $C(z, m, \mu)$ is the probability that a galaxy at redshift, z, with intrinsic apparent magnitude, m, and magnification, μ, will be detected in our magnitude limited sample and also satisfy our color selection criteria. The completeness is affected by several factors: intrinsic luminosity, dust extinction, magnification, size and IGM opacity. In the subsequent subsections, we will describe how these quantities vary and how these variations are implemented in the completeness simulations.

4.1. Simulating the Faint Galaxies

We used BC03 models to generate a template spectrum by assuming a Chabrier initial mass function, constant star formation rate, $0.2Z_{\odot}$ metallicity, and an age of 100 Myr. Both Salpeter (Salpeter 1955) and Chabrier (Chabrier 2003) initial mass functions roughly follow the
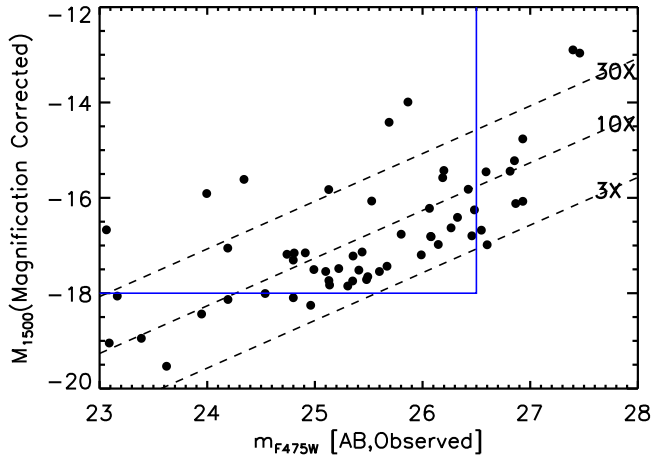
Figure 3. The intrinsic absolute magnitude, corrected for magnification, is plotted vs. observed B-band magnitude. There are 47 LBGs in the blue box which denotes galaxies that are both intrinsically faint *and* bright enough ($B < 26.5$) for follow-up ground-based spectroscopy.
(A color version of this figure is available in the online journal)

same power law for stars with $M > 1M_\odot$. However at smaller masses there are significant differences. This results in different stellar mass determinations, while having little effect on the ultraviolet spectral energy distributions.

We choose to use a somewhat younger, 100 Myr, stellar population than is typically used at these redshifts (~ 300 Myr) as the target galaxies are typically smaller and have shorter dynamical timescales than their more massive counterparts. We will present the resultant low ages from SED fitting in the near future (A. Dominguez et al., in preparation). The star formation histories are undoubtedly more complicated than the assumed constant rate, but the ultraviolet SED reacts slowly (of order 50 Myr) to sudden changes and smooths out the effects of small timescale star formation events.

Our target galaxies have low stellar masses ($7 < log(M) < 9$ $M_\odot$, A. Dominguez et al. in prep.), so we assume a lower metallicity value ($0.2Z_\odot$) than the typical value which is often used for the brighter galaxies ($1Z_\odot$). This low metallicity is justified given measurements of the mass-metallicity relation at these redshifts (Erb et al. 2006; Fynbo et al. 2008; Belli et al. 2013; Yuan et al. 2013).

We also estimated the completeness for the typical stellar population assumptions (300Myr and $1Z_\odot$) to see if varying the input stellar population parameters changes the results significantly. Our completeness determinations are robust against these initial considerations.

The Calzetti attenuation curve (Calzetti et al. 2000) was used for the dust extinction by assuming a Gaussian distribution for $E(B-V)$ centered at 0.14 (Steidel et al. 1999; Hathi et al. 2012) with a standard deviation of 0.1.

4.2. *Monte Carlo Simulation : IGM Opacity*

Ultraviolet (both Lyman emission line and continuum) photons get absorbed by neutral hydrogen clouds located along the line-of-sight to any galaxy. These intervening absorbers are classified in three groups based on their hydrogen column densities : Lyman-α forest (10^{12} cm^{-2} < N_H < $10^{17.5}$ cm^{-2}), Lyman limit systems

(LLSs, $10^{17.5}$ cm^{-2} < N_H < $10^{20.3}$ cm^{-2}) and damped Lyman-α systems (DLAs, $N_H > 10^{20.3}$ cm^{-2}). The column density distribution of these absorption clouds is given as

$$\frac{df}{dN_H} \propto N_H^{-k} \qquad (3)$$

and their number density distribution changes as a power law with redshift.

$$N(z) = N_0(1+z)^\gamma \qquad (4)$$

We have used the most updated values for k, N_0 and γ which are summarized in Table 2 (Janknecht et al. 2006; Rao et al. 2006; Ribaudo et al. 2011; O'Meara et al. 2012)

The IGM opacity at each line-of-sight is computed by running a Monte Carlo simulation. A complete description of this simulation is presented in Siana et al. (2008b). Here we briefly summarize how the IGM absorption code works.

At each redshift and for each line-of-sight to any galaxy, we select a random number from each group of intervening absorbers by sampling from a Poisson distribution with the expectation value $< N >$.

$$< N > = \int_0^{z_{galaxy}} N(z) dz \qquad (5)$$

We then select a column density and redshift for the absorber from the distributions in Equations 4 and 5, respectively. We determine the Voigt profile with doppler parameters given in Table 2, for the first twenty Lyman lines for each absorber. Finally, the IGM transmission for non-ionizing UV wavelengths at each line of sight is derived by adding the optical depths of randomly selected absorbers. We also incorporate the opacity to Lyman continuum photons using the photo-ionization cross section of $\sigma = 6.3 \times 10^{-18}$ cm^2 and decreasing as λ^3 for $\lambda < 912$ Å . We generated 1000 lines-of-sight at each redshift in bins of $\Delta z = 0.1$ over the required redshift range for the completeness simulation.

4.3. *Simulation: Incompleteness Correction*

We created a 3-D grid to compute the completeness as a function of redshift z, magnitude m and magnification μ. For each point in this 3-D space, the SED generated by BC03 was shifted, magnified and then attenuated by the IGM for 300 randomly selected line-of-sights. At each line-of-sight, the dust attenuation is sampled randomly from the Gaussian distribution mentioned above.

The photometric uncertainties, which can scatter the galaxies both into and out of the selection region, are assumed to have a Gaussian distribution with $\sigma \propto \sqrt{area}$. We assume a normal distribution for the galaxy sizes centered at 0.7 kpc (Law et al. 2012) with σ=0.2 kpc. At each line-of-sight, the randomly selected area is magnified by the magnification factor.

There is another important factor which can affect our completeness simulation. Charge transfer inefficiency (CTI) causes some signal to be lost during the readout. The CTI depends on the flux of the object, sky background, the distance on the detector between the object and the readout amplifier and the time of the observation (as the CTI worsens with time). This problem is

Table 2

Name	$\log(N_H)$	k^a	N_0^b	γ^b	b (km s^{-1})^c	redshift^b
Lyman-α forest	12 - 14	1.67	50.12	1.18	30	$1.9 \leq z$
			62.52	0.78	30	$z < 1.9$
	14 - 17.5	1.67	6.02	2.47	30	$1.9 \leq z$
			16.98	1.66	30	$0.7 \leq z < 1.9$
			35.4	0.13	30	$z < 0.7$
Lyman limit system (LLS)	17.5 - 20.3	1.07	0.17	1.33	70	$z < 2.6$
Damped Lyman-α system (DLA)	20.3 - 21.5	1.71	0.04	1.27	70	$z < 5$
	21.5 - 22	11.1	0.04	1.27	70	$z < 5$

[a] The values are taken from O'Meara et al. (2012)
[b] The column density distribution parameters N_0 and γ are from Janknecht et al. (2006); Ribaudo et al. (2011); Rao et al. (2006) for Lyman-α forests, LLSs and DLAs , respectively.
[c] The doppler parameter values are from Kim et al. (1997) and Moller & Jakobsen (1990)

more significant for images with very low background similar to our images in the F275W band ($\sim 0.5e^-$). Therefore CTI associated charge loses would make some galaxies fainter in the F275W band and push them inside the color selection region. We consider this issue in our completeness computations based on the analysis done in (Noeske et al. 2012) . The CTI is estimated as follows:

$$magnitude_{(corr)} = magnitude_{(uncorr)} - S\frac{Y}{2048} \quad (6)$$

where Y is the distance, the number of detector rows out of 2048, between each simulated galaxy and readout amplifier. For each line-of-sight, Y is randomly selected from a uniform distribution. S is a 2nd degree polynomial function of flux and observation date. More information related to the estimation of CTI is given in (Noeske et al. 2012). The CTI corrections are small for most of the F275W-detected objects (< 0.1 magnitudes), therefore they do not have a significant effect on the completeness results. See Section 7.5 for discussion of the possibility that CTI causes galaxies to be undetected in the F275W filter.

Therefore, at each point in the 3D grid (z, m, μ), we simulate 300 galaxies at different lines of sight with different reddening, distance from readout amplifier and noise (size) selected from the related distributions mentioned above. The completeness was computed by counting the fraction of galaxies that satisfy the same selection criteria as the real observed objects (Equation 2)

The completeness contours are given in Figure 4. The contours are plotted for two different values of magnification, $\mu = 2.5$ and $\mu = 5$ in units of magnitude which are the average and maximum predicted magnifications by the mass model for the LBG candidates in the sample. The figure indicates that the absolute magnitude completeness is obviously dependent upon the magnification. The color selection criteria represented in Section 3 is more than 90% complete between $1.9 < z < 2.1$. The average redshift of the sample is $z \sim 2$.

The redshift distribution of the sample predicted by the completeness simulation is in good agreement with the spectroscopic redshift distribution. Figure 5 shows the redshift distribution of all the objects with spectroscopic redshifts in the field together with the LBGs. Some of these spectroscopic redshifts are discussed in J.
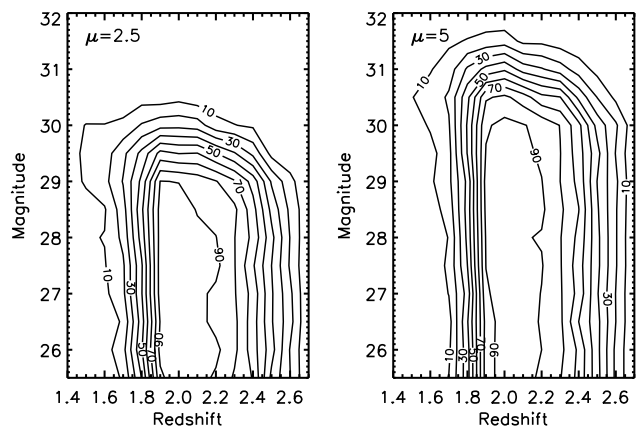
Figure 4. The completeness contours as a function of intrinsic F475W apparent magnitudes and redshifts. The contours are plotted for two values of magnification, μ=2.5 mags (the typical magnification) and $\mu = 5$ mags (an extreme magnification in our sample).

Richard et al. 2013 (in preparation). We will present the additional spectroscopic data in a future paper. We detected 79% of the galaxies in the redshift range, ($1.8 < z < 2.4$), consistent with our completeness calculations.

5. LUMINOSITY FUNCTION

The ultraviolet luminosity function at 1500 Å is measured by assuming a mean redshift of 2.0 for all of the objects. The absolute magnitudes are computed at rest-frame 1500 Å by using the apparent magnitude at F475W as below:

$$M_{1500} = m_{F475W} + \mu - 5\log(d_L/10 \text{ pc}) + 2.5\log(1+z) \quad (7)$$

Where μ is the magnification predicted by the lens model. The luminosity distribution of galaxies can be parametrized by a Schechter function which has three parameters: faint end slope (α), characteristic luminosity (L^*) and normalization coefficient (ϕ^*). We have used two methods to estimate the best values of these parameters at z $\sim$2.

5.1. V_{eff} Method

The ultraviolet luminosity function is computed using:

$$\phi(M_i)dM_i = \frac{N_i}{V_{eff}(M_i)} \quad (8)$$
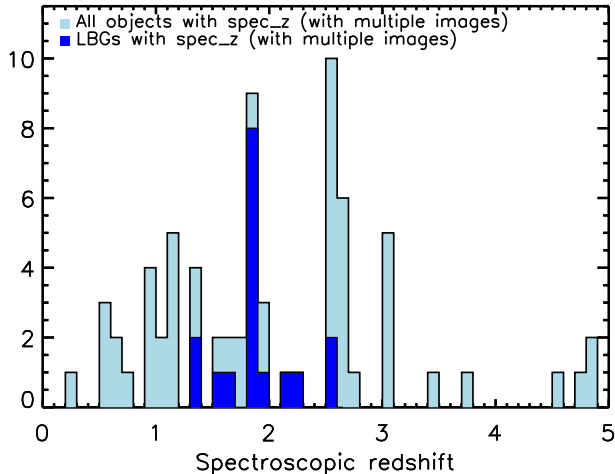
Figure 5. The spectroscopic redshift distribution. The histogram of the galaxies with spectroscopic redshift (including multiple images of the same galaxy) is shown in light blue. The dark blue histogram shows the spectroscopic redshift distribution of 17 galaxies selected as $z \sim 2$ LBGs in our image (again, including multiple images). We recovered 79% (11 of 14) galaxies in the range $1.8 < z < 2.4$ where we should have high selection completeness. A few over densities are evident at $z \sim 1.83$ and $z \sim 2.54$.
(A color version of this figure is available in the online journal)

Where N_i is the number of galaxies in magnitude bin i. V_{eff} is the effective comoving volume in which a galaxy with magnitude M can be found. The effective volume associated with each magnitude bin is derived by taking incompleteness into account,

$$V_{eff} = \sum_{\mu > \mu_0} \int_0^\infty \frac{dV_{com}}{dz} C(z, m, \mu) \Omega(\mu) \mathrm{d}z \qquad (9)$$

where $\Omega(\mu)$ is the area over which a galaxy of magnification μ can be detected in the images. Due to the distortion generated by gravitational lensing, the *total* effective area in the source plane is 0.37 arcmin² at $z \sim 2$ which is significantly smaller than the total area in the image plane. μ_0 is the minimum magnification needed for detecting an object with magnitude M relative to the magnitude limit. $C(z, m, \mu)$ is the completeness computed in Section 4.

We performed a nonlinear least squares fit to the binned number densities to simultaneously estimate the best values of the Schechter function parameters, α, M* and ϕ^*. The best fit to the luminosity function in three dimensional space of α, M* and ϕ^* was found by minimizing the sum of the residuals - the difference between the estimated number density and the value based on the model - weighted by the inverse square of the poisson error of number density in each bin. The cosmic variance doesn't affect the luminosity function results because we are dominated by Poisson errors (Subsection 5.3). The results are tabulated in Table 3.

We plotted the likelihood contours for different combinations of the Schechter parameters in Figure 6. We have estimated the parameter errors by marginalizing over these likelihood contours.

5.2. Maximum Likelihood Method
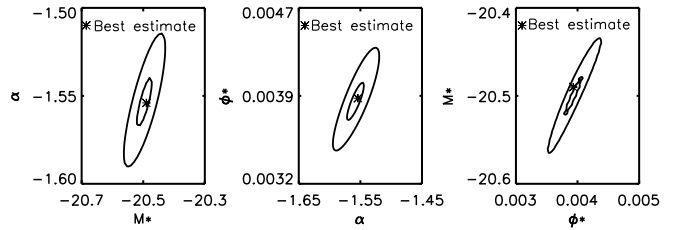
Figure 6. The 68% and 95% likelihood contours of the Schechter parameters derived from the V_{eff} method (Subsection 5.1). The best-fit values are denoted with an asterisk.

Fits to binned data are imprecise as the choice of bin size and center effects the results. Furthermore, the completeness and the effective volume can change significantly from one side of the bin to the other. The accurate approach to fitting the luminosity function is the maximum likelihood method (Sandage et al. 1979) using the individual galaxies and their associated effective volumes.

The probability that a galaxy with absolute magnitude M_i is detected in our magnitude limited sample is :

$$P(M_i) = \frac{\phi(M_i) V_{eff}(M_i)}{\int_{-\infty}^{M_{limit}} \phi(M) V_{eff}(M) \mathrm{d}M} \qquad (10)$$

Where ϕ is the parametric luminosity function and V_{eff} is found in Equation 9. M_{limit} is the faintest intrinsic absolute magnitude in the sample.

The best fit to the luminosity function was found by maximizing the joint probability which is the product of individual probabilities taken at all (unbinned) data points of the sample.

$$Likelihood = \prod_{i=1}^{N} P(M_i) \qquad (11)$$

where N is the total number of objects in the sample. In this method the normalization coefficient is canceled out so it has to be estimated separately through number counts.

$$\phi^* = \frac{N}{\int_{M_1}^{M_2} \phi(M) V_{eff}(M) \mathrm{d}M} \qquad (12)$$

Where M_1 and M_2 represent the brightest and faintest candidates in the sample, respectively, and N is the total number of galaxies in the sample.

There are two primary sources of error in the determination of the intrinsic absolute magnitudes. First, we do not know the redshift of most galaxies, so the conversion from apparent to absolute magnitude is uncertain. Using a $\Delta z = 0.25$, we derive an absolute magnitude error of $\sigma_z = 0.24$ magnitudes. Second, again due to the unknown source redshift, the magnification estimate from the mass model is uncertain. Using the same redshift uncertainty, $\Delta z = 0.25$, we find a $\sigma_\mu = 0.10$ magnitudes. The total standard deviation of the absolute magnitude (σ) is computed by adding in quadrature these two errors, σ_z and σ_μ. This uncertainty in the absolute magnitude measurement is incorporated into the analysis by marginalizing over the probability distribution of each object's magnitude. The conditional probability that a galaxy with magnitude M is in the sample, given the to-

Alavi et al.
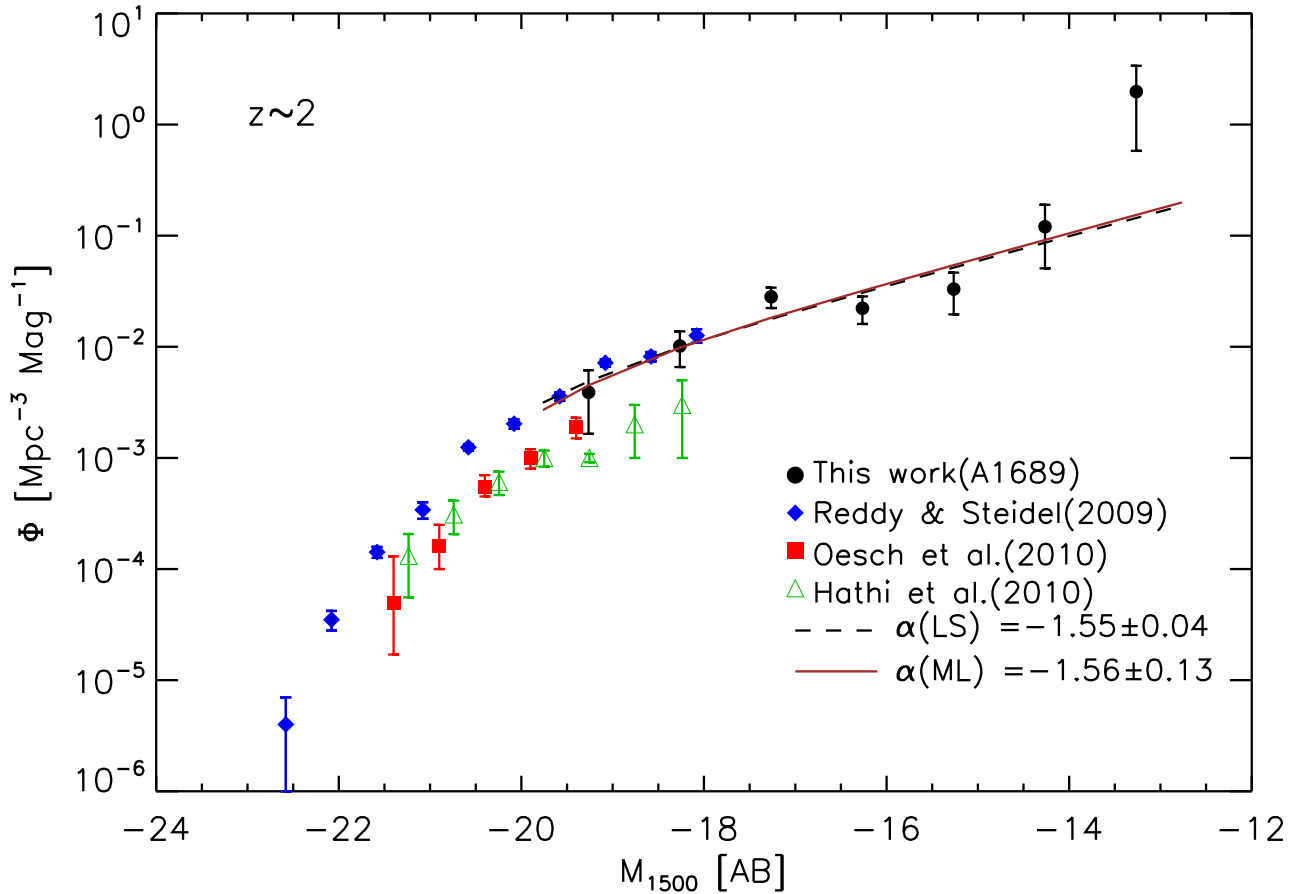
Figure 7. The UV luminosity function at z~2. The black circles are our binned luminosity function values measured by the V_{eff} method. The blue diamonds , red squares and green triangles are the LFs from Reddy & Steidel (2009), Oesch et al. (2010a) and Hathi et al. (2010), respectively. The black dashed line represents our least squares fit to our binned data and that of Reddy & Steidel (2009). The solid brown line is the best estimate of the faint end slope from maximum likelihood approach which is derived only from our data. (A color version of this figure is available in the online journal)

Table 3
UV Luminosity Function Parameters

Method	z	alpha	M*	ϕ^* (Mpc^{-3} mag^{-1})
Minimum-χ^2	2	-1.55±0.04	-20.49±0.07	0.0039±0.0005
Maximum Likelihood[a]	2	-1.56±0.13	$\cdots$	$\cdots$

[a] Maximum likelihood fit is only to our data at faint end.

tal uncertainty (σ) can be estimated through marginalization,

$$P(M_i|\alpha,\sigma) = \int_{-\infty}^{\infty} P(M_i|\mu,\alpha,\sigma)P(\mu|\sigma)\mathrm{d}\mu \quad (13)$$

where $P(M_i \mid \mu,\alpha,\sigma)$ is the Schechter function at magnitude M_i and the probability of each magnification measurement is given by a normal distribution.

$$P(\mu|\sigma) = \frac{1}{\sqrt{2\pi}\sigma}e^{\frac{-(\mu-\mu_i)^2}{2\sigma^2}} \quad (14)$$

where the mean value, μ_i, is the magnification assigned to each candidate by using the ratio of source and im-

age plane luminosities from the Abell 1689 mass model (Limousin et al. 2007; Coe et al. 2010) and assuming an average redshift $z = 2$ for all of the objects.

Assuming a prior probability for M^* from Oesch et al. (2010a) of $M^* = -20.16 \pm 0.52$, we marginalized the joint probability over M^* to find the best estimate of the faint-end slope, $\alpha = -1.56 \pm 0.13$. In this approach, we fit to only our data so the resultant value is independent of other studies. This technique was used to put a constraint only on the faint-end slope and not M^* and ϕ^* which need the data from the bright end to be estimated. Figure 7 shows the final results of the luminosity function derived with these two methods and previous determinations (Reddy & Steidel 2009; Hathi et al. 2010; Oesch et al. 2010a).

5.3. *Cosmic Variance*

The cosmic variance uncertainty $\sigma_{\rm CV}$ in the galaxy number counts can be estimated through the effective volume of the survey, the survey geometry, and an estimate of the typical clustering bias of the discovered sources. In what follows, we compute the cosmic variance uncertainty for the lensed field.

The effective volume of our survey has been calculated using the methods described in Subsection 5.1. We use these effective volumes and the selection function of the survey with redshift to determine the root-mean-squared (RMS) density fluctuations σ_ρ expected in our survey volume given its pencil beam geometry, following the methodolgy of Robertson (2010). We find these density fluctuations to be $\sigma_\rho \approx 0.1$, which is determined largely by the line-of-sight extent of the pencil beam survey (the comoving radial distance over the redshift range $1.75 \leq z \leq 2.35$ where our selection is efficient) and the linear growth factor $D(z \sim 2) \approx 0.4$.

To determine the cosmic variance uncertainty in the galaxy counts, we perform a simple abundance matching calculation (e.g., Conroy et al. 2006; Conroy & Wechsler 2009) assigning galaxies in our survey approximate halo masses and clustering bias based on their volume abundances. For galaxies in our survey, the estimated bias is $b \sim 1.2 - 2.6$, providing a cosmic variance uncertainty of $\sigma_{\rm CV} \approx 0.12 - 0.25$, comparable to or slightly larger than our fractional Poisson uncertainty $1/\sqrt{N} \approx 0.13$. We therefore expect that cosmic variance does not strongly influence the luminosity function results. Further, since cosmic variance instills a covariance in the galaxy number counts as a function of luminosity (see, e.g., Robertson 2010), if our survey probes either an over- or under-dense region compared to the cosmic mean the covariance in the counts should have little effect on the intrinsic shape of the luminosity function (especially at faint magnitudes where the galaxies are nearly unbiased tracers of the dark matter). Our faint-end slope determination is therefore expected to be robust against systematic considerations owing to cosmic variance uncertainties.

6. UV SPECTRAL SLOPE

The ultraviolet continuum of galaxies can be estimated as a power law, $f_\lambda \propto \lambda^\beta$ (Calzetti et al. 1994). The UV spectral slope, β, of each galaxy in our sample was estimated by making fake power law spectra over a wide range of β values and convolving these spectra with the filter curves. We then have a one-to-one map of the observed color to the spectral slope. We use the F475W and F625W filters to measure the UV spectral slope as they correspond to rest-frame wavelengths of ~ 1580 Å and ~ 2080 Å respectively, at $z \sim 2$. The uncertainty of the β estimate for each individual object was derived by using the photometric error in both the F475W and F625W filters.

The $E(B-V)$ values, which have a one to one relation with UV spectral slopes, are obtained based on the comparison of observed UV colors with the colors predicted from the stellar population synthesis model (BC03) and reddened with a Calzetti attenuation curve (Calzetti et al. 2000). We used the realistic assumptions for the age (100 Myr) and the metallicity (0.2 $Z_\odot$) of these compact faint galaxies (see Section 4.1). In order
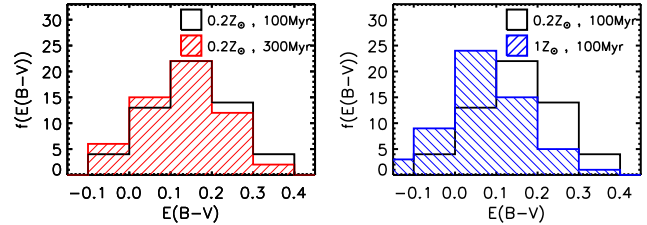
Figure 8. The $E(B-V)$ distributions of the $z \sim 2$ LBG sample. The $E(B-V)$ values are derived by comparing the LBG colors with the dust reddened colors predicted by stellar population models. The black distribution is computed by assuming the realistic values for the age (100 Myr) and metallicity (0.2 $Z_\odot$) of the stellar population models (see Section 6). The red (left panel) and the blue hatched histograms (right panel) show the $E(B-V)$ values measured by assuming (0.2 $Z_\odot$ & 300 Myr) and (1 $Z_\odot$ & 100 Myr), respectively. The assumed age of the galaxy (left) has little effect on the derived reddening values, whereas the assumed metallicity (right) has a very large effect. If we were to assume solar metallicity, a large fraction of galaxies would have colors consistent with no extinction at all.

to compare the importance of the age and metallicity in the color excess measurements, we also estimated the $E(B-V)$ values considering the more typical assumptions for these two quantities (1 $Z_\odot$ & 300 Myr). We present the color excess $E(B-V)$ distributions for three sets of age and metallicity assumptions, [(0.2 $Z_\odot$ & 100 Myr), (0.2 $Z_\odot$ & 300 Myr), (1 $Z_\odot$ & 100 Myr)] in Figure 8. The black histogram shows the distribution resulting from the realistic assumptions for the age and metallicity ($Z = 0.2Z_\odot$ and age= 100 Myr). We see that varying the assumed metallicity (right panel, blue distribution) dominates the effect on the determined reddening distribution, whereas changing the assumed starburst age has little effect (left panel, red distribution). Therefore, assuming a value of 1 $Z_\odot$ would underestimate the dust content of these faint galaxies.

In Figure 9 we plot the estimated UV slopes versus absolute magnitude at 1500 Å. The UV spectral slope, β, correlates with the UV magnitude, M_{1500}, such that the less luminous galaxies are bluer. The same trend has been identified in other works at higher redshifts and higher luminosities (Meurer et al. 1999; Labbé et al. 2007; Overzier et al. 2008; Wilkins et al. 2011; Bouwens et al. 2012b). Fitting the estimated β values versus UV luminosities, we find β=(-0.17±0.01)M_{1500}+(-4.5±0.2) for our z~2 dropout sample. We note that we removed one galaxy from our sample when fitting the reddening distribution as this galaxy had an anomalously high F625W flux. Therefore the derived reddening was quite high, even though the photometry in other bands suggested a blue spectrum.

7. DISCUSSION

We have extended the UV luminosity function at $z \sim 2$ to the faintest magnitude limit ever obtained ($M_{1500} \sim -13$), allowing us to put a strong constraint on the ultraviolet luminosity density at the epoch of peak star formation. In the next few subsections, we will discuss the contribution of faint galaxies to the ultraviolet luminosity and star formation densities at $z \sim 2$. We will also discuss the evolution of the faint-end slope of the luminosity function and dust extinction derived from the UV spectral slope, in comparison with other results from the literature.
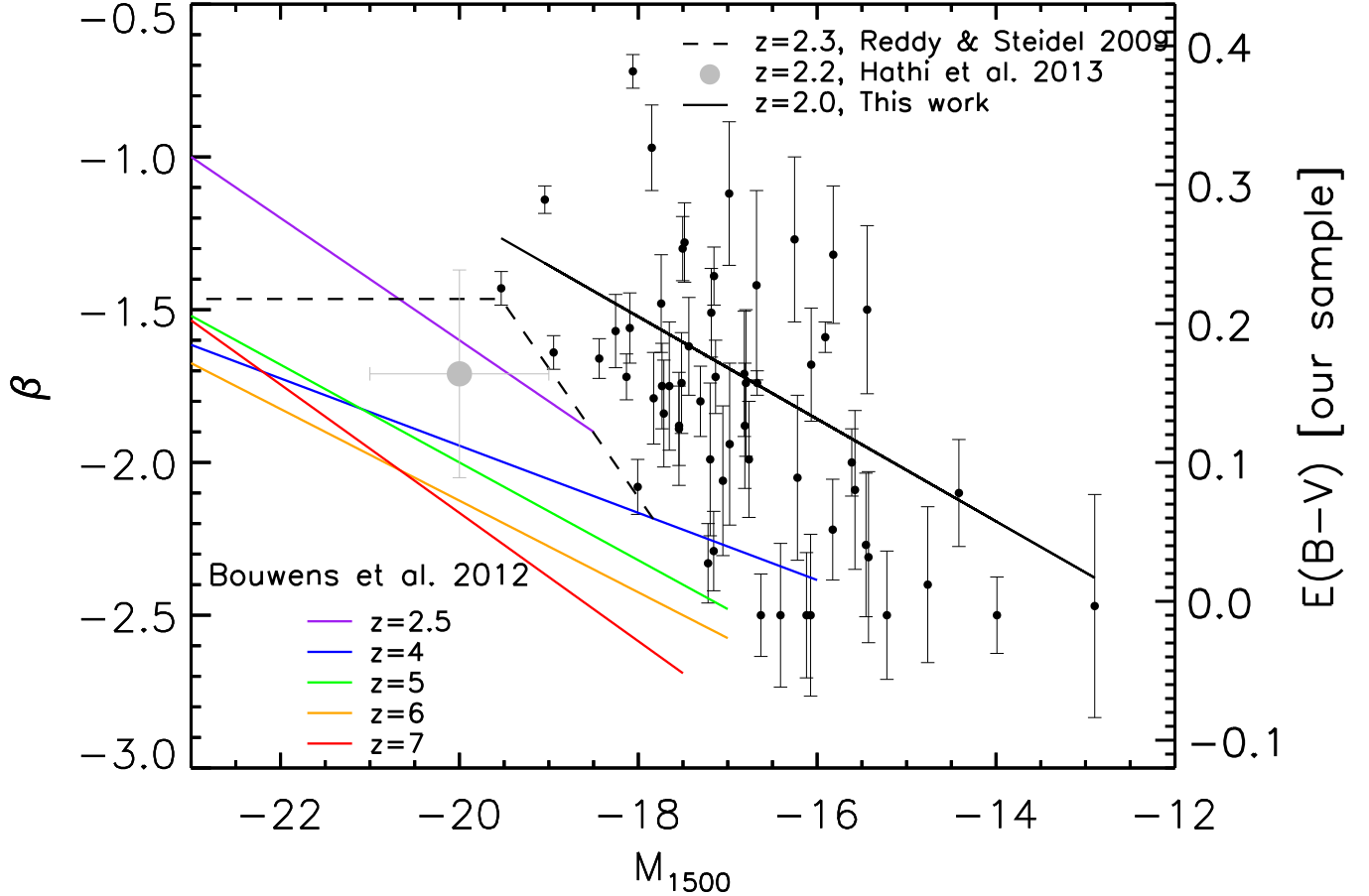
Figure 9. UV spectral slope as a function of absolute UV magnitude at 1500 AA . The black solid line is the best linear fit to the individual data. The dashed line is from Reddy & Steidel (2009) . The purple, blue, green, orange and red lines are the best linear fit for redshifts 2.5, 4, 5, 6 and 7 respectively, from Bouwens et al. (2012b). The grey point shows the average and dispersion of values measured by Hathi et al. (2013) at $z \sim 2$. The equivalent $E(B - V)$ (see text),shown on the right-hand axis, is only for the assumed values of age (100 Myr) and metallicity ($0.2Z_\odot$) assumed for our faint sample and should not necessarily be used for the other brighter samples. (A color version of this figure is available in the online journal)

7.1. Comparison with Other $z \sim 2$ Space Densities

In Figure 7, we plot our binned luminosity function with those of Reddy & Steidel (2009); Oesch et al. (2010a); Hathi et al. (2010). We prefer to compare our luminosity function with those of Oesch et al. (2010a); Hathi et al. (2010), as the galaxies are selected via a Lyman break in the same F275W filter and will therefore have similar redshift distributions. The Reddy & Steidel (2009) sample is selected with optical data alone and is at a slightly higher average redshift ($z \sim 2.3$). Given the significant evolution in the luminosity function at these redshifts (Oesch et al. 2010a), a direct comparison with the Reddy & Steidel (2009) data is not ideal but the data are plotted for reference.

If we assume that the faint-end of the luminosity function is truly a power-law, then the fits to that power law suggest an excess of moderately bright galaxies ($M_{UV} \sim -19$) in our sample compared to the measurements of Oesch et al. (2010a) and Hathi et al. (2010), though the space densities are consistent within the 1σ uncertainties. We note that both of these measurements (Oesch et al. 2010a; Hathi et al. 2010) are from the same data, a 50 arcmin^2 area in the GOODS-South region as part of the

HST Wide-Field Camera 3 Early Release Science (ERS) data (Windhorst et al. 2011).

The slightly larger space densities in our sample compared to Oesch et al. (2010a) and Hathi et al. (2010) may also be due to sample variance in both samples. Both the ERS bright galaxy sample and our sample are from single, small area fields. Though the ERS UV data covers eight times the area of our survey, they are also probing more massive galaxies, which are more highly biased and subject to sample variance. We see in Figure 5 that there are a large number of galaxies at $z = 1.83$, which may be boosting our numbers relative to the ERS sample. Surveys in additional fields are needed to address the sample variance at both the bright and faint end of the LF.

7.2. Evolution of the Faint-End Slope

Using strong gravitational lensing, we have extended the measurement of the space density of $z \sim 2$ galaxies two orders of magnitude fainter than previous studies, allowing a more accurate measure of the faint-end slope of the UV luminosity function. In Figure 10, we compare our measurement of the faint-end slope with re-

sults at other redshifts. We plotted our estimate from the maximum likelihood method as it is computed by fitting to our data alone. A general implication of this plot is that α is steeper at high redshifts than at lower redshifts. The evolution of the faint-end slope is slow between $2 < z < 7$, however it has evolved significantly between $z = 2.3$ ($\alpha \sim -1.73$ Reddy & Steidel 2009) and the present ($\alpha \sim -1.2$ Wyder et al. 2005). Our faint-end slope measurement, $\alpha = -1.56$, is a little shallower than the estimates at $z \geq 2.3$, but consistent within the error bars. This may signify the beginning of the decline in the faint-end UV spectral slope from $z \sim 2$ to the present day. Additional sight lines and deeper selection of UV galaxies at $z \sim 1$ will help us constrain the evolution of the faint end slope over the last 10 Gyr.

7.3. *Evolution of Dust in Faint Star-Forming Galaxies*

In Figure 9 we show the β vs. M_{UV} relation of our sample (black line) and similarly selected samples at higher redshift (Reddy & Steidel 2009; Hathi et al. 2013; Bouwens et al. 2012b). We see the same trend that is seen at higher redshifts in that fainter galaxies have bluer UV spectral slopes. The measured slope of the trend, $\partial\beta/\partial M_{UV} = -0.17 \pm 0.01$, is similar to the slopes measured at higher redshift, though the zeropoint is offset such that galaxies of the same UV luminosity are redder at later epochs. This is consistent with the trend seen from $2.5 < z < 7$ (Bouwens et al. 2012b). The increase in β at the same absolute magnitude from $z \sim 2.5$ to $z \sim 2$ (time difference of ~ 600 Myr) is about 0.4, consistent with the increase in beta from $z \sim 4$ to $z \sim 2.5$ (time difference of ~ 1 Gyr).

The luminosity-dependent UV spectral slope of Reddy & Steidel (2009) (derived from their reddening estimates) is also plotted in Figure 9 (dashed line). Our fitted line comes very close to their constant value of β at $M_{UV} \sim -19.5$ and consistent with the average value measured by Hathi et al. (2013) at the same redshift. The difference is that Reddy & Steidel (2009) see bluer galaxies than our average sample at $-19.5 < M_{UV} < -18$. In the faintest bin, $M_{UV} \sim -18$, Reddy & Steidel (2009) state that the colors are consistent with no dust extinction.

We believe that there are two explanations for the redder average spectral slopes exhibited in our sample compared to the Reddy & Steidel (2009) sample. First, there is a 400 Myr time difference between the average redshift of the Reddy & Steidel (2009) sample ($z = 2.3$) and our sample ($z = 2$), and we know that galaxies of the same luminosity are getting redder with time. Second, we are likely less biased against detecting red galaxies at these absolute magnitudes. Our Lyman break selection is more complete than selections like BM/BX (Adelberger et al. 2004), which purposely target galaxies that are blue in all filters. Also, our ultra-deep imaging along with the high magnification allows us to detect redder, fainter objects at higher S/N in the bluest bands.

The ultimate goal in measuring the UV spectral slopes of these galaxies is to infer the extinction of the ultraviolet light in order to measure the intrinsic UV luminosities and star formation rates. On the right axis of Figure 9 we show the implied color excess, $E(B-V)$, given the intrinsic spectral slope of our fiducial model (constant star formation, age = 100 Myr, $Z = 0.2Z_\odot$) and assuming

a Calzetti attenuation curve. We stress that the labeled $E(B-V)$ values are only valid for these assumed stellar population parameters and are therefore only applicable to our faint sample. More luminous galaxies are generally more massive and have higher metallicity.

Intriguingly, nearly every galaxy brighter than $M_{UV} < -15$ has significant reddening. The average color excess of our sample, $< E(B-V) > = 0.15$ is similar to the value measured for much more luminous galaxies by Reddy & Steidel (2009, $E(B-V) = 0.13$) and Hathi et al. (2013, $E(B-V) = 0.15$), who assumed solar metallicity in the fits to the spectral energy distributions.

The measured reddening of our sample is strongly dependent on the assumed stellar population parameters, as they affect the intrinsic UV spectral slope. This is exhibited in Figure 8, where we show that changing the metallicity of the stellar population from 1.0 $Z_\odot$ to 0.2 $Z_\odot$ decreases the average color excess from $E(B-V) = 0.15$ to $E(B-V) = 0.08$. The assumed starburst age has very little effect (average $E(B-V) = 0.15$ to $E(B-V) = 0.13$ when increasing the age from 100 to 300 Myr).

We believe that our assumed metallicity, $Z = 0.2\,Z_\odot$, is justified given the low stellar masses of our sample galaxies ($7 < \log(M^*[M_\odot]) < 9$, Dominguez et al., in prep.) and the metallicity measurements at high and low mass at these redshifts (Erb et al. 2006; Belli et al. 2013), assuming that stellar and gas-phase metallicities are similar. Thus, we come to the important conclusion that the trend of bluer UV spectral slopes at fainter absolute magnitudes is *not* necessarily due to decreasing dust reddening. Rather, the dust reddening at faint magnitudes ($-18 < M_{UV} < -15$) is similar to the reddening in more luminous galaxies ($-21 < M_{UV} < -18$), and the bluer observed UV slopes are due to bluer *intrinsic* UV slopes because the stellar population is metal poor. Of course, the reddening likely depends on luminosity as well. In order to know the exact relation of average extinction with luminosity, we need a more accurate measure of the luminosity- (or mass) metallicity relation. Furthermore, this analysis has assumed a Calzetti attenuation curve. There is some evidence that young galaxies may have steeper attenuation curves (e.g. SMC, Siana et al. 2008a, 2009; Reddy et al. 2010). Measurements of the infrared luminosities of these faint galaxies will help determine which attenuation curve is more appropriate.

In the future, measurements of metallicities (with rest-frame optical spectroscopy) and infrared luminosities will help us better understand the extinction in these faint galaxies. Because of the high magnification, these galaxies comprise an ideal sample for follow-up.

7.4. *The Effect of Intracluster Dust*

In this study, all the UV-dropouts are located behind a massive cluster so the light coming from these background galaxies can be affected by intracluster dust. Recent studies of SDSS clusters (Chelouche et al. 2007; Bovy et al. 2008; Muller et al. 2008) have shown that there is a negligible amount of intracluster dust attenuation $E(B-V) \sim 10^{-3}$ on scales of Mpc from the cluster center. We estimated the average intracluster dust reddening(A_λ) in the UV and optical bands to see if it has any effect on our LBG selection or spectral slope estimates. We approximated the A_λ values
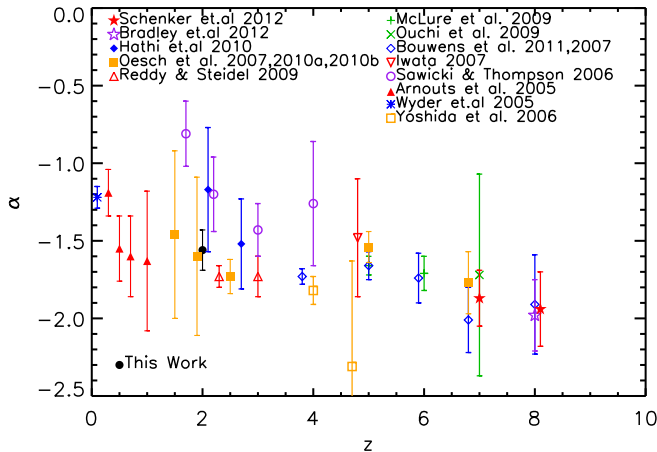
Figure 10. The evolution of the faint-end slope with red-shift. We include our maximum likelihood measurement of α (black filled circle). The plot also includes other determinations from the literature (Arnouts et al. 2005; Wyder et al. 2005; Sawicki & Thompson 2006; Yoshida et al. 2006; Bouwens et al. 2007; Iwata et al. 2007; Oesch et al. 2007; McLure et al. 2009; Ouchi et al. 2009; Reddy & Steidel 2009; Oesch et al. 2010a,b; Hathi et al. 2010; Bradley et al. 2012; Schenker et al. 2012). The data points at z=8 are all at the same redshift but have been offset slightly for clarity.
(A color version of this figure is available in the online journal)

based on the dust extinction law presented in Bovy et al. (2008). Both the UV-dropout selection and the UV spectral slope measurements are not significantly affected by intracluster reddening because the estimated color excesses are negligible ($A_{F275W} - A_{F336W} = 7 \times 10^{-3}$, $A_{F475W} - A_{F625W} = 7 \times 10^{-3}$).

7.5. F275W Non-detections and CTI

Our completeness simulations account for the small corrections to F275W magnitudes from CTI. However, one concern is that very faint F275W fluxes near the detection limit will be lost completely due to CTI. Of the final sample of 58 sources, 11 are undetected in F275W. Most of these 11 galaxies are bright in F336W and would have bright F275W magnitudes if they were blue enough to lie outside of our selection window. Therefore, CTI can not be responsible for the non-detection in F275W. However, there are five galaxies with $F336W > 27.0$, meaning that the F275W magnitude of an LBG would have to be fainter than $F275W > 28.0$ to be selected as an LBG. For these galaxies, CTI can cause a non-detection if the galaxy is far from the readout amplifier. The galaxies are 422, 1104, 1141, 1604, and 1620 pixels from the read amplifier. It is possible that a few of the galaxies that are for from the amplifier (> 1000 pixels) may be in our sample because of CTI issues. We note however that these galaxies span a range in intrinsic UV magnitudes ($-16.98 < M_{UV} < 15.22$) where there are many galaxies per bin. Therefore, even in the worst case scenario that all four of these galaxies are low-z interlopers, the CTI concerns will not significantly affect the conclusions of this paper.

We are using two orbits of our cycle-20 program to test the effects of CTI in our F275W image and will refine our selection in the future.

7.6. UV Luminosity Density

In the following discussion we prefer to compare to the samples of Oesch et al. (2010a) and Hathi et al. (2010) because the samples are selected with similar filters and are at a similar redshift. If we integrate our luminosity function (from the maximum likelihood fit) over the luminosity range of our sample alone ($-19.76 < M_{UV} < -12.76$), we derive a UV luminosity density of $\rho_{UV} = 3.56 \times 10^{26}$ erg s^{-1} Hz^{-1} Mpc^{-3}. The integrated UV luminosity density of galaxies brighter than our sample ($M_{UV} < -19.76$) is $\rho_{UV} = 4.47 \times 10^{25}$ erg s^{-1} Hz^{-1} Mpc^{-3} using the LF of Oesch et al. (2010a). Our most luminous galaxy is about the faintest galaxy seen in the Oesch et al. (2010a) sample, so there is very little overlap in luminosities. The faint galaxies in our sample account for eight times more UV luminosity density than the brighter galaxies from Oesch et al. (2010a). If we assume the luminosity function has the same slope down to zero luminosity, integrating from our faintest bin down to zero only increases the UV luminosity density by $2.4 times 10^{25}$ erg s^{-1} Hz^{-1} Mpc^{-3}. All of these values, as well as the total UV luminosity density are given in Table 4. We note that extending the luminosity range to much larger luminosities adds a negligible amount to the UV luminosity density.

This demonstrates the power of cluster lensing to quickly uncover the primary sources of star formation at these epochs.

7.7. Star Formation Rate Density

The evolution of the star formation rate density (SFRD) has been an ongoing subject of research, especially at $1 < z < 3$ because star formation appears to have peaked at this epoch. Because of the steep faint-end slope of the LF, much of the star formation occurs in faint galaxies. Furthermore, because of the significant extinction seen in our sample, there is even more star formation in our faint sample.

Of course, because this population is not well studied, many of the typical assumptions about its stellar population are uncertain. First, as mentioned previously, the metallicity is likely significantly lower than Solar, which results in significant ($\sim 15\%$) differences in the conversion of UV luminosity density to SFRD. Second, the ages of the starburst may be significantly younger than 10^8 yr, after which the conversion to SFRD is only a weak function of the age. Indeed, the assumption of continuous star formation may not be accurate at all in these systems where supernovae are thought to be very effective at shutting down star formation on short time scales (e.g. Governato et al. 2012). Third, because the typical attenuation curve in such systems has not been well measured, the dust corrections are still not well understood. Given these caveats, we calculate below the best estimate of the SFRD from UV-selected galaxies at $z \sim 2$.

We use the Kennicutt (1998) conversion of the UV luminosity density to SFR as below:

$$SFR(\ M_\odot \ yr^{-1}) = 1.4 \times 10^{-28} L_{UV} \ (erg \ s^{-1} Hz^{-1}) \quad (15)$$

where a Salpeter initial mass function from 0.1-100 $M_\odot$ is assumed. Using the total UV luminosity density from Table 4, we find a SFRD uncorrected for dust of

Table 4
UV Luminosity Density

Study	Range[a]	UV Luminosity Density[b]
Oesch et al. 2010	[-21.65,-19.76][c]	4.47
This work	[-19.76,-12.76]	35.6
Faint Extrapolation	[-12.76,0.00]	2.4
Total	[-21.65,0.00]	42.5

[a] Absolute magnitudes at 1500 Å.
[b] units of 10^{25} erg s^{-1} Hz^{-1} Mpc^{-3}
[c] The Oesch et al. (2010a) limit is slightly fainter, but we only integrate to our bright limit

0.060 $M_{\odot}$ yr^{-1} Mpc^{-3}. To correct for extinction, we note that the average attenuation measured in our sample ($E(B - V) = 0.15$) is similar to the values measured at the bright end by Reddy & Steidel (2009) and Hathi et al. (2013). Thus, we use this constant value to derive a factor of 4.17 correction for extinction (assuming a Calzetti attenuation curve) for galaxies of all luminosities. We therefore determine a SFRD of 0.25 $M_{\odot}$ yr^{-1} Mpc^{-3} for UV-selected galaxies at $z \sim 2$. If using a Kroupa (Kroupa 2001) or Chabrier (Chabrier 2003) IMF, one needs to divide this value by a 1.7 or 1.8, respectively to account for the decreased number of low mass stars relative to the Salpeter IMF. We convert to a Kroupa IMF (SFRD$_{Kroupa}$ = 0.147 M$_{\odot}$ yr^{-1} Mpc^{-3}) to compare to the value estimated by Reddy & Steidel (2009, , 0.122 M$_{\odot}$ yr^{-1} Mpc^{-3}). Our value is 20% higher but within their error bars. It is important to note however, that Reddy & Steidel (2009) use an average dust extinction correction factor of 1.91, less than half the correction that we use (4.17). Thus, if they implemented a constant extinction correction for all UV-selected galaxies, their estimate of the SFRD would more than double.

8. SUMMARY

The sensitive ultraviolet imaging capability of the WFC3/UVIS camera allows us to study the intermediate redshift ($1 < z < 3$) star-forming galaxies. We used the deepest near-UV images ever obtained with the HST/UVIS channel to identify ultra-faint star forming galaxies located behind the massive cluster Abell 1689. We found 58 Lyman break galaxies at $z \sim 2$ that are highly magnified due to strong gravitational lensing. The main conclusions of this work are summarized below:

1. The faint-end slope of UV luminosity function is estimated to be $\alpha = -1.56 \pm 0.13$, somewhat shallower than, but consistent with previous determinations at $z \sim 2.3$ (Reddy & Steidel 2009). This may indicate the beginning of a slow evolution toward shallower slopes at lower redshift.

2. The UV luminosity function shows no turnover down to very faint UV magnitudes ($M_{1500} \sim -13$). Galaxies of such low luminosities are required at $z > 7$ to reionize the intergalactic hydrogen and produce the high Thompson scattering optical depth to the cosmic microwave background seen by the Wilkinson Microwave Anisotropy Probe (Kuhlen & Faucher-Giguère 2012; Robertson et al. 2013). Indeed, these faint galaxies may contribute significantly to the ionizing background at moderate redshift ($z \sim 3$, Nestor et al. 2012).

3. The UV spectral slope for these LBGs at $z \sim 2$ is redder than higher redshift determinations at the same UV luminosities. The correlation between β and the rest-frame UV magnitude implies higher dust extinction in more luminous galaxies, as is seen at higher redshifts. We find evidence for significant dust extinction, average $E(B - V) \sim 0.15$, in most star-forming galaxies with $-18 < M_{UV} < -15$, in contrast with previous measurements at these redshifts (Reddy & Steidel 2009). Our finding assumes a Calzetti attenuation curve and $Z = 0.2 Z_{\odot}$ metallicity. Both assumptions need to be confirmed with further studies.

4. We derive a total UV luminosity density of 4.3×10^{26} erg s^{-1} Hz^{-1} Mpc^{-3} after integrating the UV luminosity of Oesch et al. (2010a) at the bright end, our luminosity function at the faint end, and extrapolating to zero luminosity. More than 80% of the UV luminosity density originates from the galaxies in the luminosity range covered by our sample. We estimate that no more than 6% of the UV luminosity density originates from fainter galaxies than those in our sample.

5. Assuming a constant extinction ($E[B - V] = 0.15$, UV dust correction of 4.2) for galaxies of all luminosities, we estimate the global SFRD (of UV-selected galaxies) to be 0.147 $M_{\odot}$ yr^{-1} Mpc^{-3} (Kroupa IMF). This number is dependent on many assumptions regarding the ages, metallicities and extinction curves for this faint population of galaxies. Further investigations are required to accurately determine these properties for this new population.

REFERENCES

Adelberger, K. L., Steidel, C. C., Shapley, A. E., et al. 2004, ApJ, 607, 226

Arnouts, S., Schiminovich, D., Ilbert, O., et al. 2005, ApJ, 619, L43

Belli, S., Jones, T., Ellis, R. S., & Richard, J. 2013, ArXiv e-prints

Bertin, E., & Arnouts, S. 1996, A&AS, 117, 393

Bouwens, R., Bradley, L., Zitrin, A., et al. 2012a, ArXiv e-prints

Bouwens, R. J., Illingworth, G. D., Franx, M., & Ford, H. 2007, ApJ, 670, 928

Bouwens, R. J., Illingworth, G. D., Bradley, L. D., et al. 2009, ApJ, 690, 1764

Bouwens, R. J., Illingworth, G. D., Oesch, P. A., et al. 2012b, ApJ, 754, 83

Bovy, J., Hogg, D. W., & Moustakas, J. 2008, ApJ, 688, 198

Bradley, L. D., Bouwens, R. J., Ford, H. C., et al. 2008, ApJ, 678, 647

Bradley, L. D., Trenti, M., Oesch, P. A., et al. 2012, ApJ, 760, 108

Broadhurst, T. J., Taylor, A. N., & Peacock, J. A. 1995, ApJ, 438, 49

Bruzual, G., & Charlot, S. 2003, MNRAS, 344, 1000

Bunker, A. J., Stanway, E. R., Ellis, R. S., & McMahon, R. G. 2004, MNRAS, 355, 374

Bunker, A. J., Wilkins, S., Ellis, R. S., et al. 2010, MNRAS, 409, 855

Calzetti, D., Armus, L., Bohlin, R. C., et al. 2000, ApJ, 533, 682

Calzetti, D., Kinney, A. L., & Storchi-Bergmann, T. 1994, ApJ, 429, 582

Casertano, S., de Mello, D., Dickinson, M., et al. 2000, AJ, 120, 2747

Chabrier, G. 2003, PASP, 115, 763

Chelouche, D., Koester, B. P., & Bowen, D. V. 2007, ApJ, 671, L97

Coe, D., Benítez, N., Broadhurst, T., & Moustakas, L. A. 2010, ApJ, 723, 1678

Coe, D., Zitrin, A., Carrasco, M., et al. 2013, ApJ, 762, 32

Coleman, G. D., Wu, C.-C., & Weedman, D. W. 1980, ApJS, 43, 393

Conroy, C., & Wechsler, R. H. 2009, ApJ, 696, 620

Conroy, C., Wechsler, R. H., & Kravtsov, A. V. 2006, ApJ, 647, 201

Daddi, E., Cimatti, A., Renzini, A., et al. 2004, ApJ, 617, 746

Egami, E., Kneib, J.-P., Rieke, G. H., et al. 2005, ApJ, 618, L5

Erb, D. K., Shapley, A. E., Pettini, M., et al. 2006, ApJ, 644, 813

Fynbo, J. P. U., Prochaska, J. X., Sommer-Larsen, J., Dessauges-Zavadsky, M., & Møller, P. 2008, ApJ, 683, 321

Governato, F., Zolotov, A., Pontzen, A., et al. 2012, MNRAS, 422, 1231

Hathi, N. P., Ryan, Jr., R. E., Cohen, S. H., et al. 2010, ApJ, 720, 1708

Hathi, N. P., Cohen, S. H., Ryan, Jr., R. E., et al. 2012, ArXiv e-prints

—. 2013, ApJ, 765, 88

Iwata, I., Ohta, K., Tamura, N., et al. 2007, MNRAS, 376, 1557

Janknecht, E., Reimers, D., Lopez, S., & Tytler, D. 2006, A&A, 458, 427

Jones, T., Ellis, R., Jullo, E., & Richard, J. 2010, ApJ, 725, L176

Kennicutt, Jr., R. C. 1998, ARA&A, 36, 189

Kim, T.-S., Hu, E. M., Cowie, L. L., & Songaila, A. 1997, AJ, 114, 1

Kneib, J.-P., Ellis, R. S., Santos, M. R., & Richard, J. 2004, ApJ, 607, 697

Koekemoer, A. M., Fruchter, A. S., Hook, R. N., & Hack, W. 2003, in HST Calibration Workshop : Hubble after the Installation of the ACS and the NICMOS Cooling System, ed. S. Arribas, A. Koekemoer, & B. Whitmore, 337

Kroupa, P. 2001, MNRAS, 322, 231

Kuhlen, M., & Faucher-Giguère, C.-A. 2012, MNRAS, 423, 862

Labbé, I., Franx, M., Rudnick, G., et al. 2007, ApJ, 665, 944

Law, D. R., Steidel, C. C., Shapley, A. E., et al. 2012, ArXiv e-prints

Lilly, S. J., Le Fevre, O., Hammer, F., & Crampton, D. 1996, ApJ, 460, L1

Limousin, M., Richard, J., Jullo, E., et al. 2007, ApJ, 668, 643

Madau, P. 1995, ApJ, 441, 18

Madau, P., Ferguson, H. C., Dickinson, M. E., et al. 1996, MNRAS, 283, 1388

Magnelli, B., Elbaz, D., Chary, R. R., et al. 2011, A&A, 528, A35

McLure, R. J., Cirasuolo, M., Dunlop, J. S., Foucaud, S., & Almaini, O. 2009, MNRAS, 395, 2196

Meurer, G. R., Heckman, T. M., & Calzetti, D. 1999, ApJ, 521, 64

Moller, P., & Jakobsen, P. 1990, A&A, 228, 299

Muller, S., Wu, S.-Y., Hsieh, B.-C., et al. 2008, ApJ, 680, 975

Narayan, R., Blandford, R., & Nityananda, R. 1984, Nature, 310, 112

Nestor, D. B., Shapley, A. E., Kornei, K. A., Steidel, C. C., & Siana, B. 2012, ArXiv e-prints

Nestor, D. B., Shapley, A. E., Steidel, C. C., & Siana, B. 2011, ApJ, 736, 18

Noeske, K., Baggett, S., Bushouse, H., et al. 2012, WFC3 UVIS Charge Transfer Eciency October 2009 to October 2011, Tech. rep.

Oesch, P. A., Stiavelli, M., Carollo, C. M., et al. 2007, ApJ, 671, 1212

Oesch, P. A., Bouwens, R. J., Carollo, C. M., et al. 2010a, ApJ, 725, L150

Oesch, P. A., Bouwens, R. J., Illingworth, G. D., et al. 2010b, ApJ, 709, L16

Oke, J. B., & Gunn, J. E. 1983, ApJ, 266, 713

O'Meara, J. M., Prochaska, J. X., Worseck, G., Chen, H.-W., & Madau, P. 2012, ArXiv e-prints

Ouchi, M., Mobasher, B., Shimasaku, K., et al. 2009, ApJ, 706, 1136

Overzier, R. A., Bouwens, R. J., Cross, N. J. G., et al. 2008, ApJ, 673, 143

Pettini, M., Rix, S. A., Steidel, C. C., et al. 2002, Ap&SS, 281, 461

Pickles, A. J. 1998, VizieR Online Data Catalog, 611, 863

Rao, S. M., Turnshek, D. A., & Nestor, D. B. 2006, ApJ, 636, 610

Reddy, N. A., Erb, D. K., Pettini, M., Steidel, C. C., & Shapley, A. E. 2010, ApJ, 712, 1070

Reddy, N. A., & Steidel, C. C. 2009, ApJ, 692, 778

Reddy, N. A., Steidel, C. C., Fadda, D., et al. 2006, ApJ, 644, 792

Ribaudo, J., Lehner, N., & Howk, J. C. 2011, ApJ, 736, 42

Richard, J., Kneib, J.-P., Ebeling, H., et al. 2011, MNRAS, 414, L31

Richard, J., Stark, D. P., Ellis, R. S., et al. 2008, ApJ, 685, 705

Rix, H.-W., Barden, M., Beckwith, S. V. W., et al. 2004, ApJS, 152, 163

Robertson, B. E. 2010, ApJ, 713, 1266

Robertson, B. E., & Ellis, R. S. 2012, ApJ, 744, 95

Robertson, B. E., Furlanetto, S. R., Schneider, E., et al. 2013, ArXiv e-prints

Salpeter, E. E. 1955, ApJ, 121, 161

Sandage, A., Tammann, G. A., & Yahil, A. 1979, ApJ, 232, 352

Sawicki, M., & Thompson, D. 2006, ApJ, 642, 653

Schenker, M. A., Robertson, B. E., Ellis, R. S., et al. 2012, ArXiv e-prints

Siana, B., Teplitz, H. I., Chary, R.-R., Colbert, J., & Frayer, D. T. 2008a, ApJ, 689, 59

Siana, B., Polletta, M. d. C., Smith, H. E., et al. 2008b, ApJ, 675, 49

Siana, B., Smail, I., Swinbank, A. M., et al. 2009, ApJ, 698, 1273

Stark, D. P., Ellis, R. S., Richard, J., et al. 2007, ApJ, 663, 10

Stark, D. P., Swinbank, A. M., Ellis, R. S., et al. 2008, Nature, 455, 775

Steidel, C. C., Adelberger, K. L., Giavalisco, M., Dickinson, M., & Pettini, M. 1999, ApJ, 519, 1

Steidel, C. C., Pettini, M., & Hamilton, D. 1995, AJ, 110, 2519

Tanvir, N. R., & Levan, A. J. 2012, Memorie della Societa Astronomica Italiana Supplementi, 21, 46

Trenti, M., Perna, R., Levesque, E. M., Shull, J. M., & Stocke, J. T. 2012, ApJ, 749, L38

Wilkins, S. M., Bunker, A. J., Stanway, E., Lorenzoni, S., & Caruana, J. 2011, MNRAS, 417, 717

Windhorst, R. A., Cohen, S. H., Hathi, N. P., et al. 2011, ApJS, 193, 27

Wyder, T. K., Treyer, M. A., Milliard, B., et al. 2005, ApJ, 619, L15

Yan, H., Dickinson, M., Giavalisco, M., et al. 2006, ApJ, 651, 24

Yan, H.-J., Windhorst, R. A., Hathi, N. P., et al. 2010, Research in Astronomy and Astrophysics, 10, 867

Yoshida, M., Shimasaku, K., Kashikawa, N., et al. 2006, ApJ, 653, 988

Yuan, T.-T., Kewley, L. J., & Richard, J. 2013, ApJ, 763, 9

Zheng, W., Postman, M., Zitrin, A., et al. 2012, Nature, 489, 406

Zitrin, A., Moustakas, J., Bradley, L., et al. 2012, ApJ, 747, L9